Tunability of exchange bias in Ni@NiO core-shell nanoparticles obtained by sequential layer deposition

Tunability of Exchange Bias in Ni@NiO Core-Shell Nanoparticles Obtained by Sequential Layer Deposition

Maria Chiara Spadaro[1,2], Sergio D'Addato[*1,2], Paola Luches[1], Sergio Valeri[1,2], Vincenzo Grillo[1,3], Enzo Rotunno[3], Manuel A. Roldan[4,5], Stephen J. Pennycook[6], Anna Maria Ferretti[7], Elena Capetti[7] and Alessandro Ponti[7]

[1]CNR-NANO, via G. Campi 213/a, 41125 Modena, Italy

[2]Dipartimento FIM, Università di Modena e Reggio Emilia, via G. Campi 213/a, 41125 Modena, Italy

[3]CNR-IMEM, Parco Area delle Scienze 37/A - 43100 Parma, Italy

[4]Departamento Física Aplicada III, Facultad de Ciencias Físicas, Universidad Complutense de Madrid, Ciudad Universitaria, 28040 Madrid, Spain.

[5]Materials Science and Technology Division, Oak Ridge National Laboratory, P.O. Box 2008 Oak Ridge, TN 37831

[6]Department of Materials Science and Engineering, National University of Singapore, Singapore, 117576

[7]Laboratorio di Nanotecnologie, Istituto di Scienze e Tecnologie Molecolari, Consiglio Nazionale delle Ricerche, via G. Fantoli 16/15, 20138 Milano (Italy)

*E-mail:sergio.daddato@unimore.it.

Abstract. Films of magnetic Ni@NiO core-shell nanoparticles (NPs, core diameter d ≅ 12 nm, nominal shell thickness variable between 0 and 6.5 nm) obtained with sequential layer deposition were investigated, to gain insight into the relationships between shell thickness/morphology, core-shell interface, and magnetic properties. Different values of NiO shell thickness t_s could be obtained while keeping the Ni core size fixed, at variance with conventional oxidation procedures where the oxide shell is grown at the expense of the core. Chemical composition, morphology of the as-produced samples and structural features of the Ni/NiO interface were investigated with spectroscopy (XPS) and microscopy (SEM, TEM) techniques, and related with results from magnetic measurements obtained with SQUID. The effect of the shell thickness on the magnetic properties could be studied. The exchange bias (EB) field H_{bias} is small and almost constant for t_s up to 1.6 nm, then it rapidly grows, with no sign of saturation. This behavior is clearly related to the morphology of the top NiO layer, and is mostly due to the thickness dependence of the NiO anisotropy constant. The ability to tune the EB effect by varying the thickness of the last NiO layer represents a step towards the rational design and synthesis of core-shell nanoparticles with desired magnetic properties.

Keywords: core/shell nanoparticles, Ni, NiO, exchange bias, physical synthesis, TEM, SQUID

1. Introduction

Research on magnetic metal-oxide core-shell nanoparticles (NPs) has been extensively carried out during the last decade, as their fields of application encompass many areas, like nanomedicine, medical imaging, refrigeration, spintronics and recording industry [1,2]. Fabrication of NPs at progressively decreasing size with desired properties (like for instance thermal stability and pre-determined coercivity values), has been certainly one of the most important challenges in this research field. In fact, the superparamagnetic (SPM) limit [3,4] may be an obstacle for the production of smaller stable magnetic NPs: as an example, from the definition of blocking temperature $T_B = KV/(25k_B)$ [5], it can be estimated that, for an anisotropy constant $K = 0.5 \cdot 10^4$ J/m^3 (typical value of Ni [6]), T_B is equal to room temperature (RT) when a NP has critical volume $V_{crit} = 2.1 \cdot 10^4$ nm^3, corresponding to a SPM blocking diameter $d \approx 34$ nm. In order to stabilize smaller NPs, an Antiferromagnetic (AFM) shell can be generated around the Ferromagnetic (FM) core, creating an AFM/FM exchange coupling at the core/shell interface (Exchange Bias, EB) [2-5]. Tunability of this effect can be achieved with careful control of the parameters affecting the NP growth and the subsequent physical properties (core/shell structure, metal/oxide interface quality, shell thickness and oxide composition). For instance, this method was extensively applied to Co@CoO NPs [2-4]: the NPs were oxidized in order to obtain metal core/oxide shell and deposited on a substrate. It was found that at increasing in-plane coverage (i.e., NP surface density) there is an increase of T_B, of coercivity and of exchange bias field, due to "recovery" of magnetic properties caused by the neighboring oxide shells coming into contact and providing a more efficient exchange interaction with the FM cores [2-4]. Different methods of core/shell NPs preparation have been implemented: chemical synthesis [1,7], lithography, self-assembling [8,9], atom deposition and thermally assisted precipitation in a matrix [10].

Synthesis of NPs by using magnetron gas-aggregation sources, followed by their deposition onto a substrate, allows the necessary systematic and accurate investigation [11-13] of the dependence of NP properties on their size and morphology. Moreover, there is the advantage of producing ligand-free NPs in a clean environment, as the sources operate in vacuum. Co-deposition of different species with thermal evaporation sources, in order to obtain core-shell geometry with non-native oxide shells, or NPs embedded in a solid matrix [12,14-15], allowed a systematic study of the effect of shell thickness and composition on the NP assembly properties. In a recent paper by D. Llamosa et al. [16] complex core@shell and core@shell@shell NPs were obtained by a modified gas aggregation source, similar to the one used in the present work and in previous studies, but cores and shells were only metallic.

Magnetic stabilization induced by EB can be obtained in Ni@NiO NP because of the high Néel temperature value of NiO (T_N= 525 K) [6]. Recent experiments have been carried out on Ni [17] and Ni@NiO [18,19] NPs generated by a gas aggregation source, with the linear size d ranging between 4 and 8 nm. Their structure, morphology, and stability to air exposure were deeply investigated with a number of techniques. These studies showed that the metallic core of the produced NPs had a regular multi-twinned icosahedral structure, composed of single-crystal tetrahedra with (111) faces, and that after controlled oxidation, oxide shells were obtained, with the presence of crystalline NiO oxide islands on the NP facets, with direct or twinned stacking [19]. The obtained NPs were found chemically and structurally stable and, in particular, the Ni core maintained its metallic nature even after prolonged exposure to atmospheric conditions (more than 20 days)[17]. Recently, the influence of different oxidation procedures on the magnetic properties of preformed Ni NPs was reported on [20].

In most of the recent works on exchange bias and interface magnetic couplings in core-shell NPs, the external oxide shell was obtained by oxidizing partially the original NP, either chemically or thermally[21]. In this way, the oxide shell is created at the expense of the core, and reduction of the core size has to be taken into account when the results of experimental studies on the magnetic properties are evaluated [4]. In the present paper, results of a structural, morphological and magnetic characterization of Ni@NiO NPs are presented, focusing on a preparation method where pre-formed Ni NPs and NiO "layers" were sequentially deposited. By varying the amount of deposited NiO, it was possible to obtain NPs with constant core linear size and different shell thickness, at variance with the procedures where the shell was obtained by oxidizing the original NPs. In this way, a systematic investigation of the EB and coercive fields as a function of the shell thickness could be carried out.

For a thorough investigation of the NP films, a number or techniques have been employed: X-ray Photoelectron Spectroscopy (XPS) for an analysis of Ni/NiO chemical composition, Scanning Electron Microscopy (SEM) for NP films morphology, High Resolution (HR)-TEM and Scanning Transmission Electron Microscopy (STEM) for NP structure. In particular, the Exit Wave Reconstruction (EWR) method for HR-TEM image analysis [22,23] was used, which allowed a software correction of the lens aberrations and therefore a more direct determination of atom locations as compared with conventional techniques. An analysis of the SEM images could give information about the core diameter and shell thickness of the obtained NP films. The same samples analyzed in SEM and XPS were also used for magnetic measurements. The magnetic parameters of the Ni@NiO core-shell NPs were obtained by analyzing the field-cooled isothermal magnetization (hysteresis loops) and the thermal magnetization curves in Field

Cooled/Zero Field Cooled (FC/ZFC) modes measured by a Superconducting Quantum Interference Device (SQUID) magnetometer.

2. Experimental

The Ni@NiO NP films were prepared in an experimental system with three interconnected vacuum chambers [15, 18, 18]. The first chamber was equipped with a NP source (NC200U, Oxford Applied Research) and a Quadrupole Mass Filter (QMF). In the source, Ni atoms were evaporated by magnetron sputtering, and they were condensed into NPs by an inert gas carrier (in our case, Ar) [17]. The charged NPs in the produced beam were mass selected by the QMF, and could enter the deposition chamber, where they were deposited on a substrate. Deposition could occur in O_2 atmosphere (which was let in by a leak valve). NiO films were obtained by evaporating Ni from a thermal evaporator in presence of O_2 ($p_{O2} = 2 \cdot 10^{-7}$ mbar). The deposition rate of the different materials was monitored with a quartz microbalance. Figure 1 shows a sketch of the experimental system source and of the deposition chambers, with the used NP source and metal evaporators.

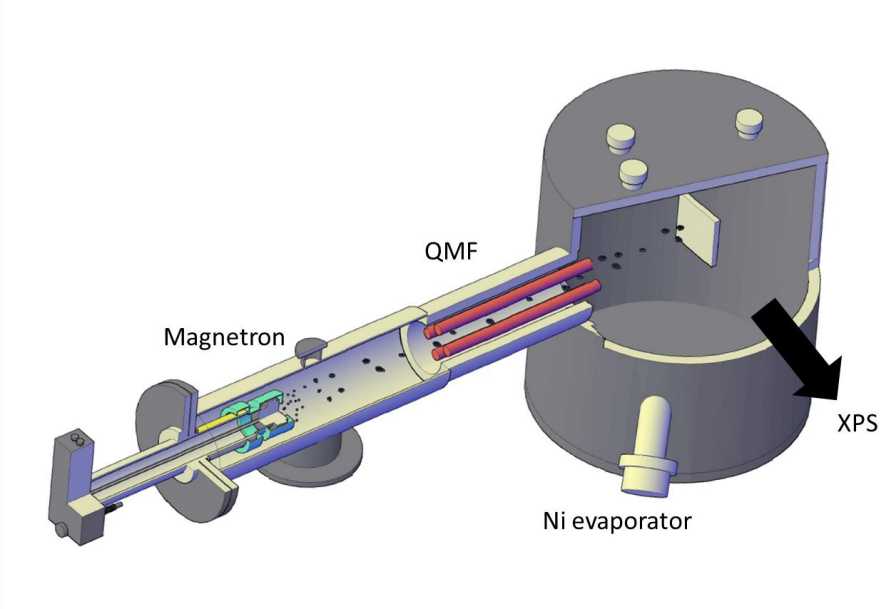

Figure 1a. Sketch of the experimental system used for core/shell NP growth. A beam of mass-selected metal Ni NPs was generated with a gas aggregation source, consisting of a magnetron evaporator, a gas aggregation region and a quadrupole mass filter (QMF). The beam impinged on a substrate. Shells surrounding the pre-formed Ni NPs were realized by sequential deposition of a first layer of NiO, a second layer of metal Ni NPs, and a third layer of NiO. NiO layers were obtained by thermal evaporation of Ni in presence of O_2 in the deposition chamber.

After deposition, the sample could be transferred *in vacuum* to the third chamber, equipped with an Al-Mg twin anode X-ray source (XR50, Specs), generating Al K_α photons ($h\nu$ = 1486.7 eV), and an electron hemispherical analyzer (Phoibos 150, Specs) for *in situ* XPS analysis [15,18]. During the experiments reported in this work, the samples were produced with a NP beam generated with a magnetron discharge power P = 35 W, and Ar flow f = 50 sccm. In these conditions we could obtain Ni NPs with a linear size distribution between 8 and 15 nm, as directly verified by analyzing the SEM images, as discussed in the following section (the size distribution of the deposited particles was always checked *ex-situ* with SEM). The amount of deposited Ni NPs and of NiO (see the results discussion) are given in this work in terms of the nominal thickness of an equivalent continuous film with the same density as bulk fcc Ni (t_{Ni}) and rock-salt NiO (t_{NiO}). Therefore, the units for equivalent thickness and deposition rate values are respectively nm and nm/min. Inert substrates were used during the experiments, in particular Si/SiO_x for SEM, XPS and SQUID, and carbon-coated copper grids for TEM and STEM. SEM images were acquired with a dual beam system (FEI Strata DB235M). The SEM column is equipped with a Schottky field-emission gun, achieving a resolution of 2 nm, which is nominally constant over the energy range employed in this work (5-15 keV) [17]. The HR-TEM and some

of the STEM experiments were performed using a JEOL JEM-2200FS working at 200KeV and equipped with Schottky Field emission Gun (SFEG) and Ω-filter for energy loss analysis [15, 18-20]. The instrument has an objective lens spherical aberration coefficient of 0.5 mm, permitting a point to point resolution of 0.19 nm. In order to remove delocalisation effects focal series of 20 images have been acquired and processed with IWFR software [22,23]. The series were acquired for focal steps between 10 and 15 nm starting from close to Scherzer conditions. The exact defoci have been determined for each image by detailed semi-automatic fitting of the amorphous rings within STEM CELL [24]. A series of STEM images were obtained also with an aberration corrected STEM, Nion UltraSTEM 200 working at 200kV located at Oak Ridge National Laboratory, USA. Probe deconvolution was used in STEM image analysis [24]. Magnetization measurements were carried out by a Quantum Design MPMS XL-5 SQUID magnetometer. Field Cooled (FC) and Zero-Field Cooled (ZFC) thermal magnetization curves were recorded in the 5 – 300 K range with cooling field H_{cool} = 100 Oe and measuring field H_{meas} = 100 Oe. Magnetization isotherms were recorded between +2000 Oe and –2000 Oe at 5 K after field cooling (H_{cool} = +2000 Oe). The data were corrected for support diamagnetism [25,26] and, in the case of magnetization isotherms, scaled to the nominal deposited nickel mass.

3. Results and discussion.

The NP films were obtained by depositing trilayer films, NiO /Ni NPs/ NiO, where the first and third layer of NiO were obtained by a flux of Ni atoms coming from a thermal evaporator, in O_2 atmosphere (samples labeled as “TriL”). For comparison, Ni@NiO NP assemblies were also

obtained by annealing metallic Ni NPs in air at T=250 °C for t= 30 min (sample labeled as "Ann")[20].

The TriL samples were prepared with fixed nominal thickness of the first layer ($t_{1,NiO}$= 1 nm) and of the second layer (composed of Ni NPs, with $t_{2,Ni}$= 6 nm) but with increasing nominal thickness of the third layer from $t_{3,NiO}$ = 0 to 6.5 nm. The first layer of NiO was deposited in order to have a NiO/Ni NP interface beneath the Ni cores, too, thus completing the NiO shells around the deposited Ni NPs. Evidence of formation of core-shell NPs was provided by SEM, HR-TEM and STEM images. As an example, a STEM image of NI@NiO NPs is reported in Figure 2. The NPs show a defined core-shell structure, with core linear size *d* between 8 and 12 nm, while the shell thickness t_s varies between 2 and 3 nm.

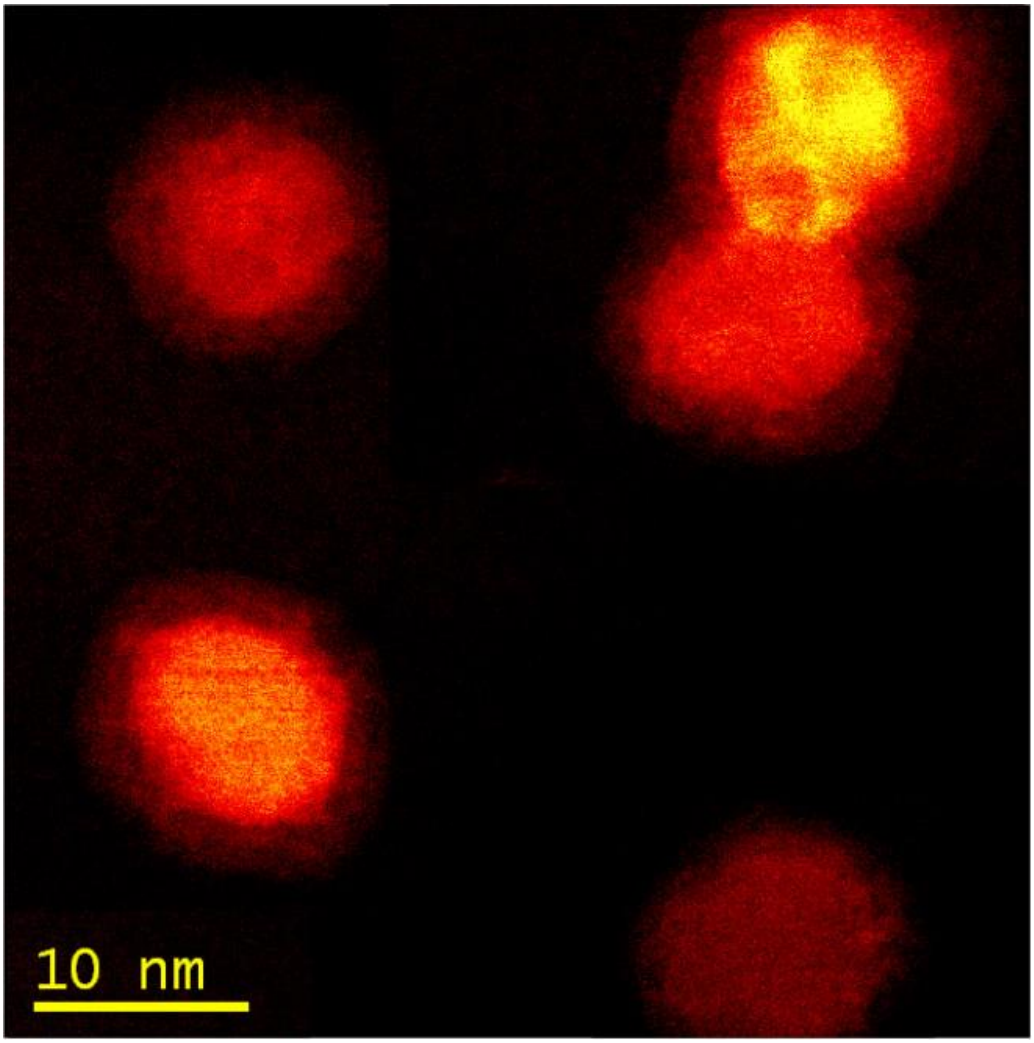

Figure 2. STEM image in false colors of Ni@NiO NPs obtained by sequential layer deposition. The core shows bright while the shell is seen as a faint halo.

3.1 Chemical composition

The samples were then analyzed with XPS, focusing on Ni 2p core level spectra. In this way information on the chemical state of Ni atoms from the outmost layers of the films could be extracted, in order to monitor in situ the formation of the oxide shells [18]. As an example, fig 3a

reports Ni 2p spectra measured on TriL samples after each deposition step (evaporated Ni in O_2, metallic Ni NPs, evaporated Ni in O_2). The spectra show the typical doublet manifold, corresponding to emission from $2p_{3/2}$ and $2p_{1/2}$ core levels, with satellite structures due to final state effects occurring in the photoemission process [18]. The spectrum labeled NiO, acquired after deposition of the first layer, strongly resembles that of stoichiometric NiO, previously reported in the literature [27]. In particular, peak A (Binding Energy, BE=853.7 eV) and a shoulder labeled S (at about 2.5 eV higher BE from A) are clearly visible: this double feature was assigned to emission from well coordinated Ni in stoichiometric NiO [18,27]. After deposition of preformed Ni NPs, the spectrum changes significantly, and it is now dominated by two peaks labeled B1 (BE=852.3 eV) and B2 (BE=869.7 eV), corresponding to emission from metallic Ni, although a careful inspection of the spectrum shows the presence of a shoulder corresponding to peak A (NiO), due to the uncovered areas of the underlying NiO first layer. In the spectrum acquired after the deposition of the third layer the situation is reversed: peaks A and S (stoichiometric NiO) are again dominant, with a shoulder corresponding to structure B_1 (metallic Ni). It can be inferred therefore that the first and the third layer are mainly composed of stoichiometric NiO, at variance with films composed of Ni NPs deposited in O_2 atmosphere and/or subsequently exposed to O_2, where the spectra of Ni atoms in the oxidized shell do not exhibit the typical features of well coordinated NiO [27]. The evolution of the Ni 2p core level lineshape of the complete trilayer films could also serve as a further monitor of the increasing thickness of the third NiO layer, with relative intensities of peaks A and B varying significantly (see fig. 3b).

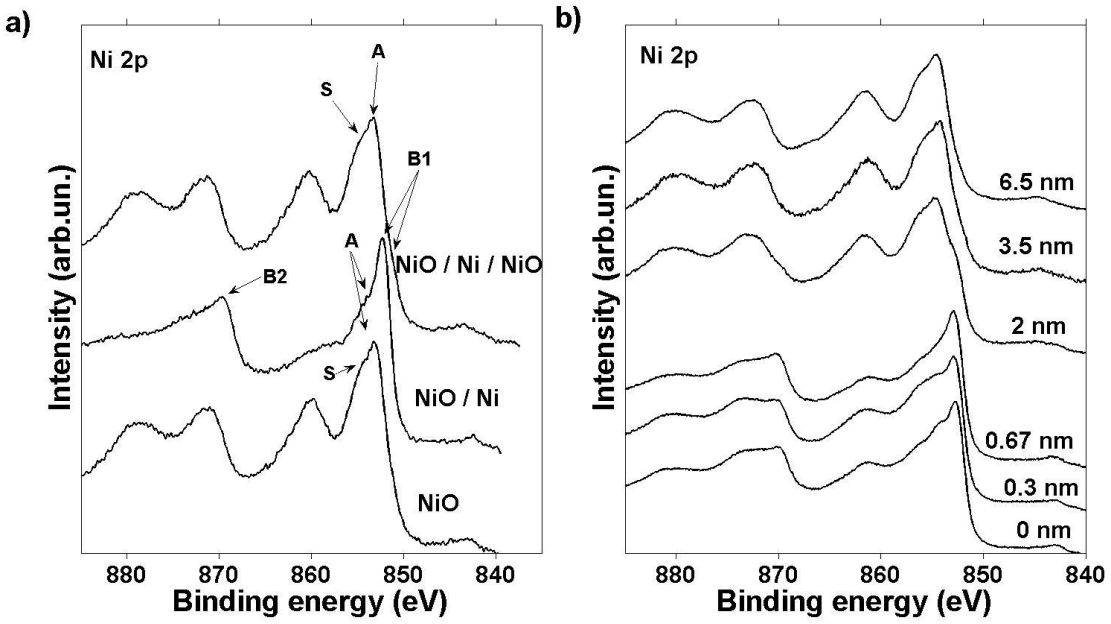

Figure 3. (a) Ni 2p core level XPS spectra measured on a trilayer NiO/Ni NPs/NiO sample (triL 3.5), after sequential deposition of the first layer of NiO, pre-formed metal Ni NPs and the third layer of NiO ($t_{3,NiO}$=3.5 nm). (b) Ni $2p_{3/2}$ XPS core level spectra measured on TriL samples at increasing third layer nominal thickness value.

3.2 Film morphology

SEM images of the obtained samples were acquired to study the film morphology. Figure 4 shows images taken from TriL samples of different 3rd layer thickness values: $t_{3,NiO}$=0 nm (Fig.4a), $t_{3,NiO}$=1 nm (Fig.4b), $t_{3,NiO}$=2 nm (Fig.4c) and $t_{3,NiO}$=6.5 nm (Fig.4d). In the image taken from the TriL 0 sample (corresponding to a film where only Ni NPs were deposited on NiO first layer) Ni NPs are clearly visible, and the sample morphology was found to be typical of the random paving growth mode [12,17]: the corresponding size distribution histogram, obtained by measuring the diameters of the NPs imaged is reported in the inset in Figure 4a. The average value of the NP diameters <d> was obtained by fitting the histogram to a log-normal distribution,

and was found to be <d>=12.0 nm, with a standard deviation σ_d = 1.0 nm. At increasing coverage of the third layer, the morphology of the film changed: the size of the NPs gradually increased, and some smaller grains could be observed, probably due to formation of NiO islands. At the highest value of third layer thickness that was investigated ($t_{3,NiO}$=6.5 nm), a discontinuous film was formed, with grains that could extend up to 60 nm. These results are a clear indication that the third NiO layer formed shells around the Ni NPs at low coverage, and on increasing $t_{3,NiO}$ the shells extended, eventually forming a solid matrix embedding the original Ni NPs.

The best-fit log-normal curves of the linear size distribution for the different trilayer samples are plotted in Figure 5a. It can be readily observed that the value of $<d>$ increases and the distribution broadens progressively with $t_{3,NiO}$. It was possible to estimate the average value of the shell thickness t_s of the NPs using the formula:

$$<t_s> = (1/2)\,(<d> - <d_0>) + t_{corr} \qquad (1)$$

where <d> is the average diameter of the NPs obtained by the analysis of the SEM images, $<d_0>$ is the NP average diameter obtained for the sample where the third NiO layer was absent, and t_{corr} is a correction value. It was necessary to introduce t_{corr} to take into account the expansion of the bare Ni NPs after some exposure to air when the sample was transferred to SEM and to SQUID instruments.

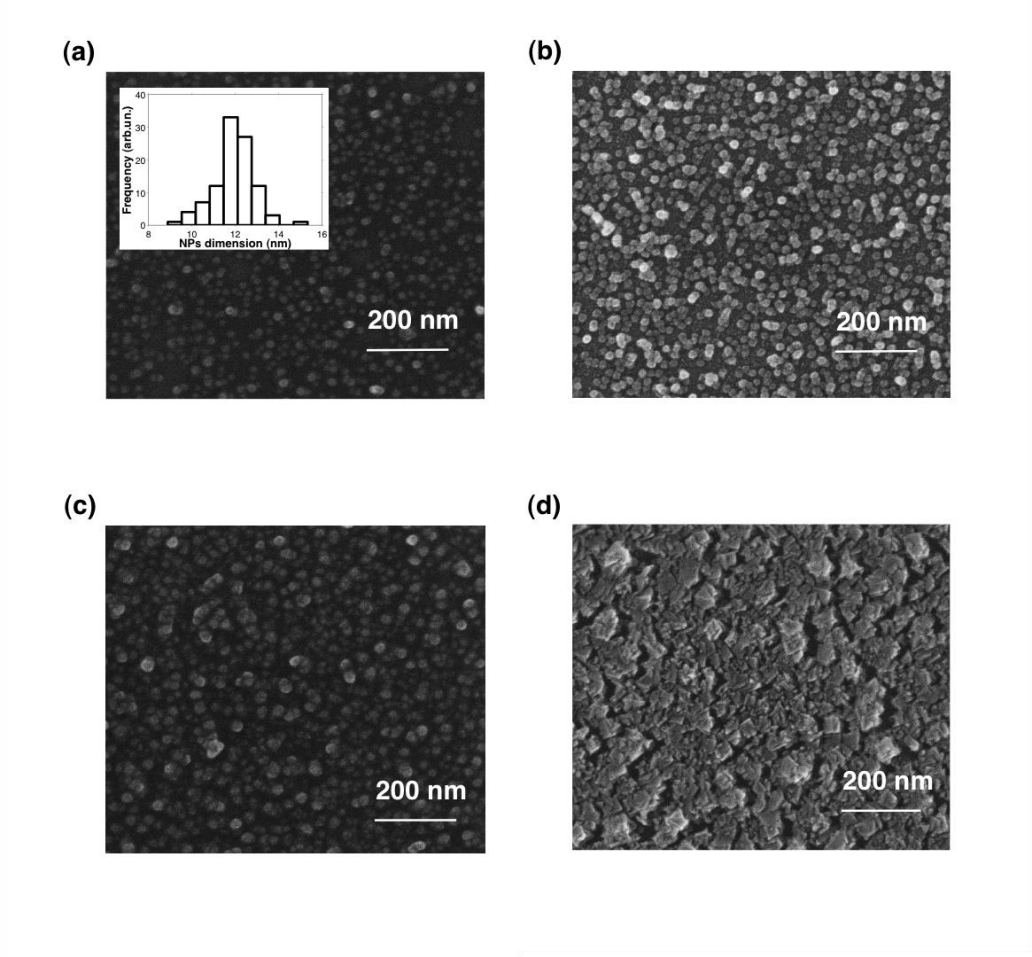

Figure 4. SEM images of selected NiO/Ni NPs/NiO TriL samples, with different values of the third NiO layer, namely: (a) TriL 0, (b) TriL 1, (b), (c) Tril 2, (d) TriL 6.5.

As the bare NPs were exposed to air, their external layers were oxidized, and this resulted in a change of their size, due to different density values of Ni and NiO. Previous TEM experiments showed that after some hours of exposure to atmosphere the NPs showed a layer of native oxide with thickness of about 1 nm [18]. Assuming that this shell (of circular shape) was made of NiO, the difference between the diameter of the exposed NPs and the original diameter of the bare NPs affected by exposure is 0.6 nm, corresponding to a correction factor t_{corr}=0.3 nm. This value

is about 3% of the value of $<d_0>$ as obtained by SEM. The values of $<d>$, σ_d, and t_s for the various samples are reported in Table 1.

Sample	$<d>$ (nm)	σ_d (nm)	t_s (nm)
TriL 0	11.96 ±0.04	0.99±0.06	-
TriL 0.3	12.35±0.02	1.08±0.02	0.5±0.1
TriL 0.67	13.38±0.03	1.42±0.03	1.0±0.1
TriL 1	14.61±0.07	1.73±0.08	1.6±0.1
TriL 2	15.97±0.03	2.29±0.06	2.3±0.1
TriL 3.5	17.89±0.07	3.26±0.11	3.2±0.1
Ann	11.27±0.07	1.13±0.06	1.5±0.2

Table 1. Average diameter $<d>$, standard deviation σ_d obtained by fitting the distribution size obtained from the grain analysis of the TriL samples to a log-normal, and estimated NiO shell thickness t_s obtained by using equation 1. The uncertainties of $<d>$ and σ_d are obtained by the fitting procedure. The uncertainty of t_s is dominated by the uncertainty in the estimated value of t_{corr}. Values of $<d>$ and σ_d of the Ann sample are also reported. In this case t_s has been estimated by averaging the NiO shell thickness of 13 NPs measured from STEM images.

The values of corrected shell thickness t_s were also plotted in Figure 5b as a function of the nominal thickness of the third layer, $t_{3,NiO}$ The data shown in Figure 5b follow a growing trend, with a change in slope at $t_{3,NiO}$ = 1.0 nm. This behavior can be ascribed to a switching from a situation where NiO preferentially grows on the metal Ni surface of the as-deposited NP, thus forming the shell, to a situation where the original NP facets are completely coated with NiO and

growth continues on the oxide shell and partially on the substrate. Complete oxide shells are formed and extend, finally developing an oxide matrix that embeds the original NP cores. This result is in agreement with previous observations on Ni@MgO [15] and FePt@MgO [28] NP films.

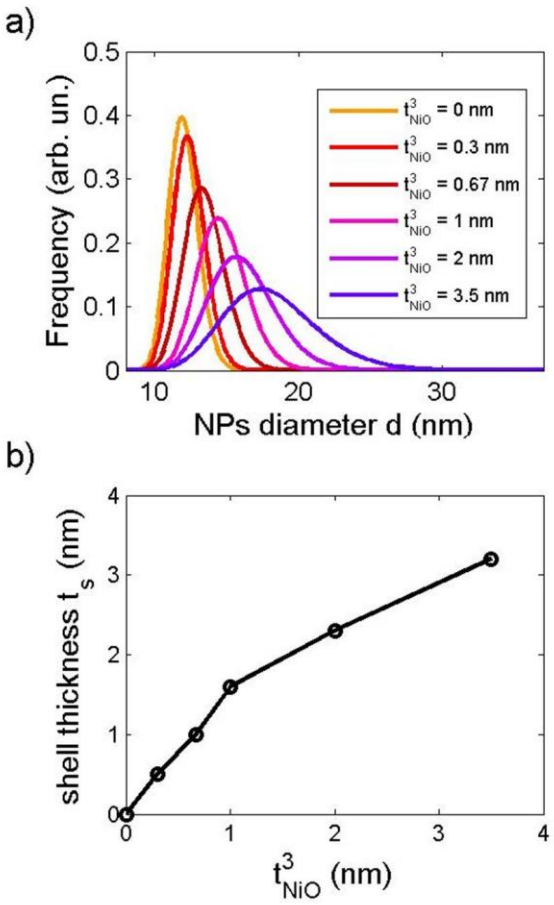

Figure 5. (a) Evolution of the NP linear size distribution fitting curves for the NiO/Ni NPs/NiO trilayer samples at increasing values of the NiO third layer nominal thickness $t_{3,NiO}$. (b) Plot of the estimated shell thickness t_s vs $t_{3,NiO}$.

3.3 Core-shell interface structure

In order to have a complete picture of the NP structure, a detailed study of the core/shell interface was carried out with HR-TEM and STEM. This study could help significantly to understand the details governing the AFM shell/FM core coupling and the EB effect. We performed the measurement on one Tril sample and on NPs annealed at T=250ºC in air (Ann sample) [20]. The nominal thickness values for the chosen TriL sample were $t_{1,NiO}$ = 1 nm, $t_{2,Ni}$ = 3 nm, $t_{3,NiO}$ = 1 nm. The chosen value of $t_{2,Ni}$ was lower with respect to samples used for SEM, XPS and SQUID experiments, in order to obtain clearer images of single preformed Ni NPs. An atomically resolved STEM image of a Ni NP after annealing in air is shown in Figure 6a. The NP clearly presents a core-shell structure. The core shape is compatible with a McKay icosahedral structure obtained by 20 tetrahedra with (111) facets, due to multiple twinning occurring during the NP growth in the gas aggregation chamber [29,30]. The same structure was obtained on Ni [18], bare FePt and core/shell FePt@MgO [28], Au and other fcc transition metals NPs [31], and is ascribed to the dynamics of NP growth. In particular, it was found that formation of icosahedra is favored at fast quenching rates for fcc metal NPs [32]. The core/shell interface of the NPs imaged in Figure 6a is sharp, and the shell is mostly crystalline NiO (rocksalt cubic structure, see figure S. 1 in supplementary material), growing in the [111] direction (see figure S.2 in supplementary material). Figure 6b shows an EWR of an HR-TEM image of a NP from the Ann sample. The Ni/NiO interface orientation was determined by measuring the change in the periodicity of the lattice fringes (from 0.21 nm to 0.24 nm), and a (111) orientation was obtained for the NiO planes, as shown in the enlarged area which is reported in Figure 6c.

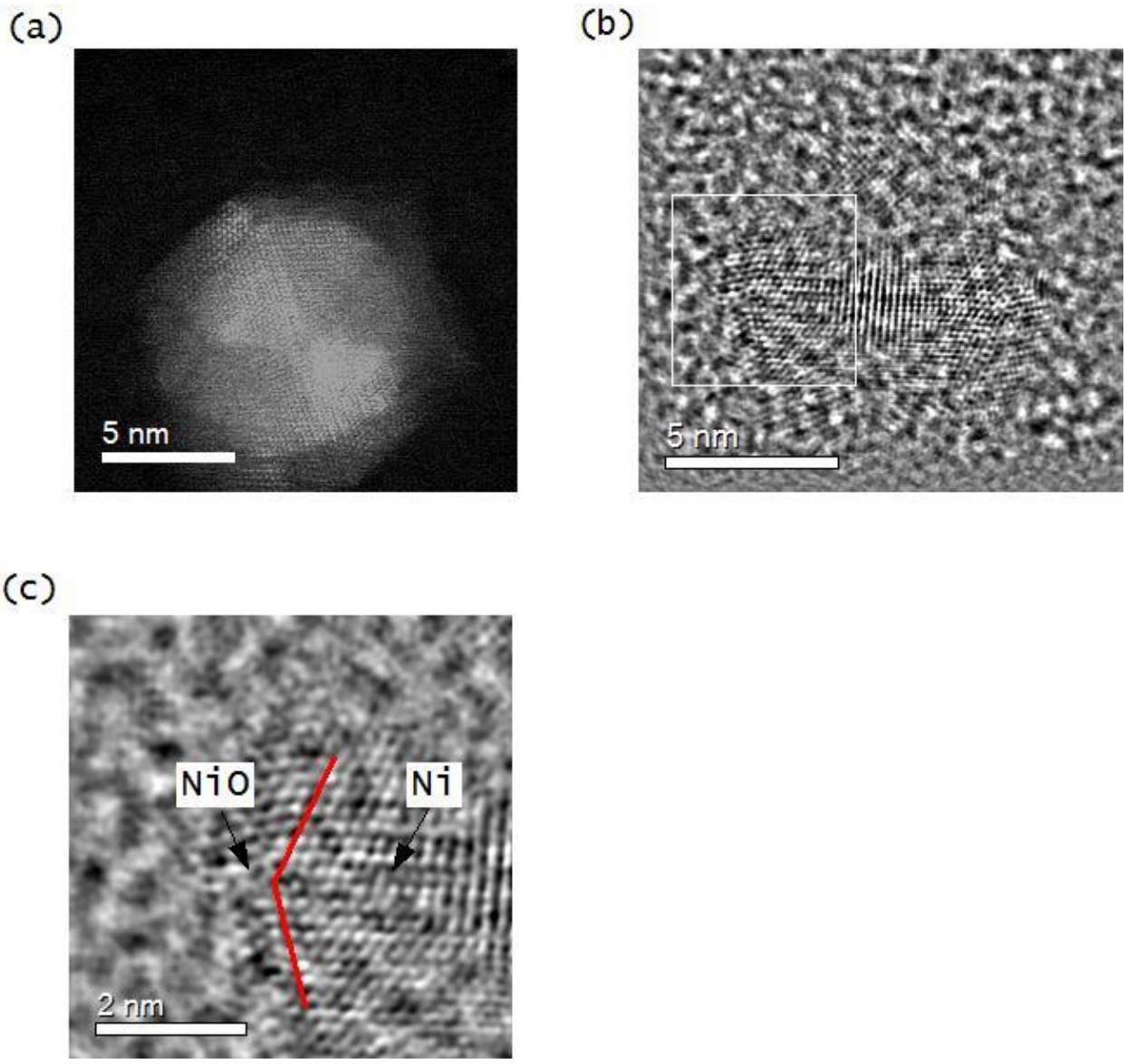

Figure 6. (a) STEM image of a Ni@NiO core-shell NP obtained by annealing in air of pre-formed metal Ni NPs assembly (sample Ann). (b) EWR image of a Ni@NiO NP from the same sample. (c) Magnified portion of the image in (b), putting in evidence the Ni/NiO interface, which was found by looking at the variation of the periodicity in the lattice fringes.

By the STEM technique, it was also possible to focus on interface details, like in the case of the image reported in Figure 7a, where two NPs are visible. A detailed analysis was performed on the enlarged area shown in figure 7b. Geometric phase analysis (GPA) and peak maxima analysis [33] obtained from this image revealed the presence of dislocations, that could accommodate the lattice mismatch between fcc Ni and rock-salt NiO (111) planes (see Figures 7c and 7d). It can be deduced that the high degree of crystal ordering in the NiO shells is probably favored by the interface stress relaxation due to high temperature of annealing, which is the origin of the dislocations. A more careful inspection of the epitaxy relations obtained by the (S)TEM images lead to the conclusions that there is a 5:6 NiO/Ni interface coincidence, assuming a 1% expansion of the NiO shell (see figure S.3 in supplementary material).

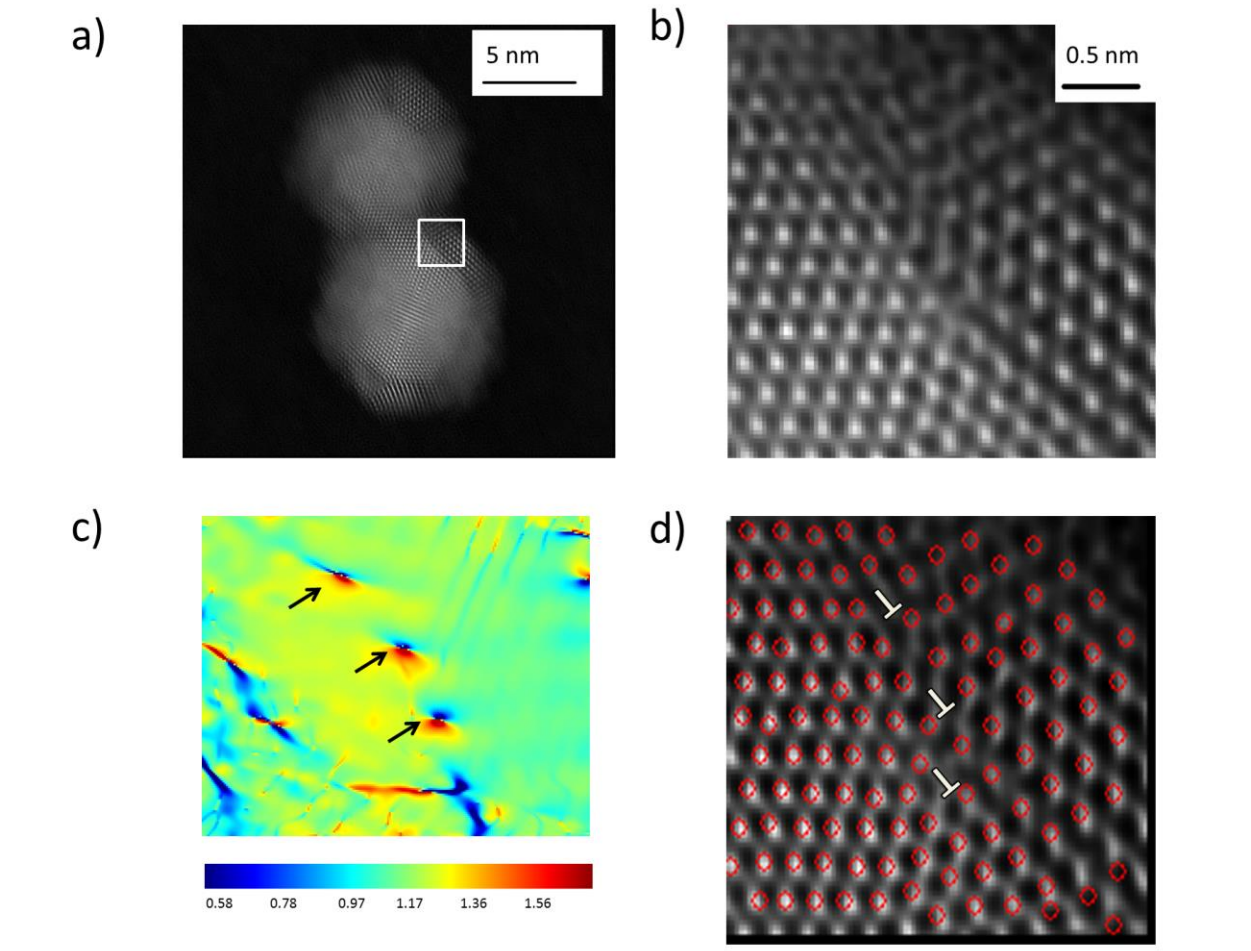

Figure 7. (a) STEM image of two Ni@NiO core-shell NPs obtained by annealing in air of a preformed Ni NP assembly (sample Ann). (b) Zoom of the area delimited by the white rectangle in (a), where the Ni/NiO interface is clearly visible. (c) GPA image of the strain eyy in the nearly vertical direction obtained from (b). The arrows indicate the dislocations located at the Ni/NiO interface. (d) Peak maxima reconstruction of the zoomed image in (b), evidencing the dislocations previously observed.

Figure 8a reports a STEM image of a TriL sample prepared for TEM experiments. The NP core-shell structure is evident also in this image, with the core having the usual McKay icosahedral shape. The main difference between this image and the one of Figure 7a is the reduced interface sharpness and the lower degree of crystal ordering of the shell. An EWR image of a single representative NP is reported in Figure 8b, where in part of the shell areas atomic fringes show a different orientation with respect to the case of Figure 6b. This arrangement is visible in the blown-up region of Figure 8c, with the corresponding simulation in Figure 8d. The shell atomic columns extending out of the interface have a periodicity corresponding to NiO (200) planes. A geometrical calculation allowed us to identify of the NiO growth direction on the Ni (111) facets as [243] (figure S.4 in supplementary material). This epitaxial relation can explain the 3:4 NiO/Ni interface coincidence observed by TEM (figures 8c and 8d) and requires 11% expansion of the NiO lattice (see figure S.5 in supplementary material). It can also be observed in Figure 8c that the phase signal at the interface is more confused than those in the core and shell regions. This result, at variance with the case of the annealed sample, confirmed that the interface in the Tril samples was less sharp than in the annealed samples. A possible explanation is that reactive deposition of Ni in O_2 on the pre-formed NPs produced less ordered oxide shells with respect to the ones prepared by annealing in air. Nevertheless, the shells in the TriL samples presented a good degree of stoichiometry, as evidenced by XPS Ni 2p core level analysis.

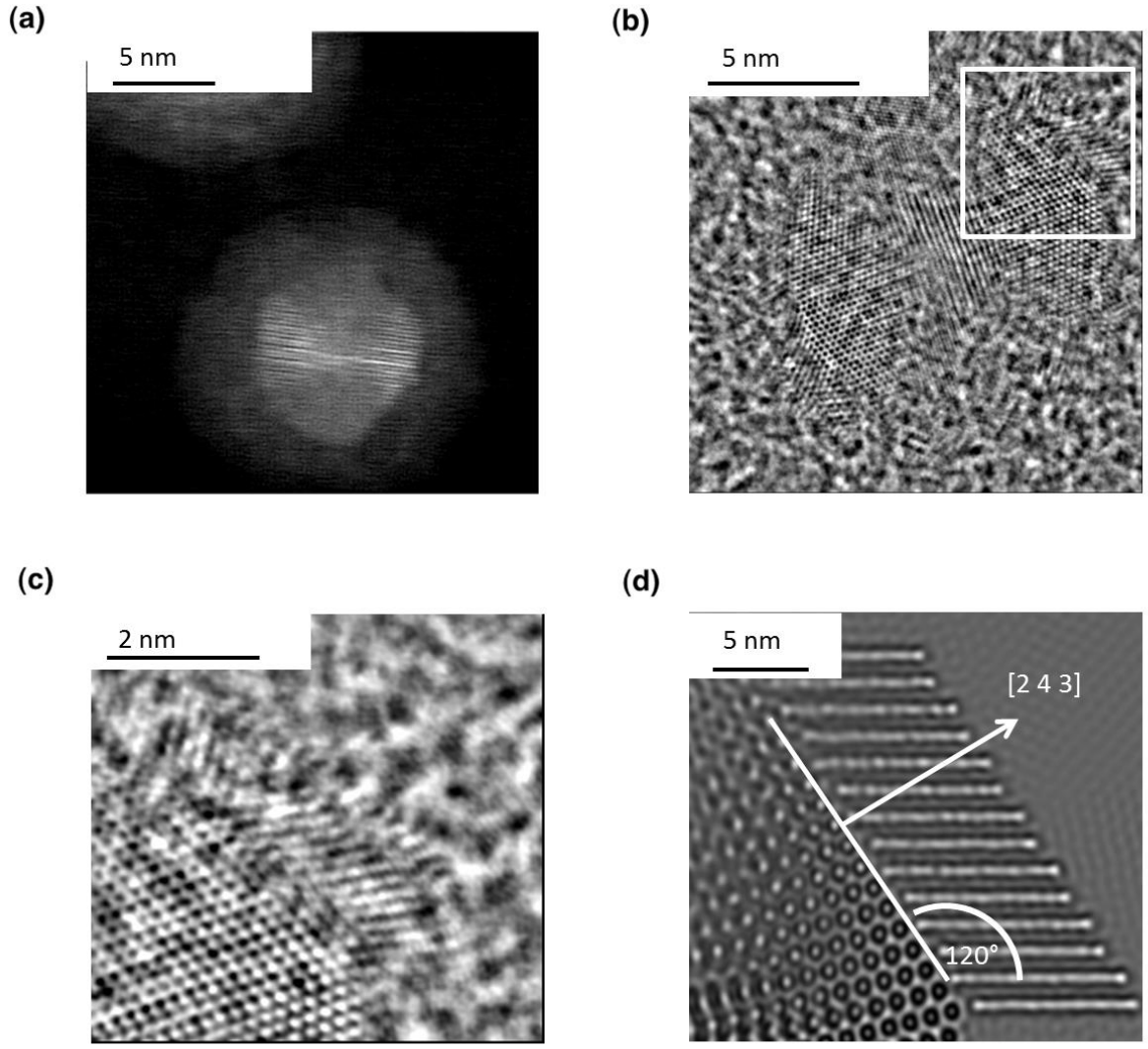

Figure 8. (a) STEM image of a NP in TriL sample, showing that the NP has a core-shell structure. In this sample, the nominal thickness values were $t_{1,NiO}$ = 1 nm, $t_{2,Ni}$ = 3 nm, $t_{3,NiO}$ = 1 nm. (b) EWR image from the same sample, where a core@shell Ni@NiO NP is shown. (c) blow-up of the interface region I (b). (d) Simulation of the region shown in (c).

3.4 Magnetic properties

The magnetic properties of the Ni@NiO core-shell NP assemblies were investigated with a focus on the influence of the shell thickness on the magnetization thermal behavior, coercivity and exchange-bias field. To provide a framework to understand the magnetic data it is useful to recall some critical diameters for ideal Ni NPs, i.e., homogeneous, spherical, non-interacting Ni NPs free from surface effects [34]. Ideal Ni NPs with diameter d < 50 nm are single domain NPs and the magnetization reversal takes place via coherent rotation. Their superparamagnetic (SPM) blocking diameter is 34 nm at RT and 9 nm at 5 K. A population of ideal Ni NPs with diameter distribution equal to that of the investigated Ni cores would have a mean blocking temperature $<T_B>$ = 15 K and standard deviation σ_{T_B} = 4 K. Hence, the ideal NPs in such population would be well into the SPM regime at RT and almost completely blocked at 5 K.

The ZFC and FC thermal magnetization curves $M_{(Z)FC}(T)$ are shown in Fig. 9. Samples TriL 0 – TriL 2 have a similar behavior that is largely different from that of TriL 6.5. TriL 3.5 shares features with both the low $t_{3,NiO}$ samples and TriL 6.5. At low temperature, M_{ZFC} and M_{FC} are different due to the aligning effect of the cooling field. The $M_{FC} - M_{ZFC}$ difference decreases upon increasing T as the growing thermal energy enables the NP magnetic moment to overcome magnetic anisotropy barriers and more favorably align towards the applied field. When $M_{FC} - M_{ZFC}$ vanishes, the NPs enter the reversible (SPM) regime. In our samples, this occurs at the temperature T_{max} where M_{ZFC} is maximum, a common estimate of the blocking temperature T_B. The samples TriL 0 to TriL 3.5 have T_{max} = 200 - 220 K, much higher than the blocking temperature expected for ideal Ni NPs of equal size. In the reversible regime (from T_{max} to 300 K), M_{ZFC} and M_{FC} are linear as previously observed [17], a behavior typical of SPM NPs coupled by exchange and magnetostatic interactions [14]. (We use the term “magnetostatic” instead of

"dipolar" since the size of the Ni core is not negligible with respect to the core-core distance, as required by the dipolar approximation). The temperature $T_{1/2}$, where M_{ZFC} reaches half of its maximum value, is another estimate of T_B. It also displays similar values in samples TriL 0 – Tril 3.5 ($T_{1/2}$ = 50 – 100 K). In samples TriL 0 – TriL 2 (but not TriL 3.5) a decrease of M_{FC} at low temperature is observed that is the signature of the formation of a collective spin-glass-like state driven by random inter-NPs interactions [35,36]. Sample TriL 6.5 has a completely different behavior. It does not reach reversibility even at 300 K and has high T_{max} > 300 K and $T_{1/2} \cong$ 190 K, indicating that the magnetic anisotropy barriers are much higher than those of the low $t_{3,NiO}$ samples. Figure 9g shows that M_{FC} is constant throughout the whole temperature range, a feature shared with TriL 3.5 at low T, showing that no spin-glass-like state exists in these samples.

The (Z)FC magnetization curves are a probe of the low-field ($H_{cool} = H_{meas}$ = 100 Oe) thermal behavior of the Ni@NiO NPs. Samples TriL 0 – TriL 3.5 have T_{max} (about 200 K) much higher than the blocking temperature of equally-sized ideal NPs [T_B = (15 ± 4) K] [36]. There is no evidence that T_B of TriL 0 – TriL 3.5 depends on the NiO shell thickness, so EB does not seem to be the cause of the high T_B. The linearity of M_{ZFC} and M_{FC} at high T suggests the presence of magnetostatic inter-NP interactions that could be responsible for the high T_B of these samples. Indeed, Ni NPs deposited on Si with similar density (Sample A in Ref. [20]) displayed T_{max} = 140 K and negligible EB, supporting the view that the T_{max} of TriL samples can mostly be ascribed to magnetostatic interactions. Sample TriL 6.5 displayed a larger T_{max} despite the Ni core size and density – and consequently the average magnetostatic interactions – being unchanged. A similar T_{max} increase has been previously observed for Co@CoO NPs in Al_2O_3 matrix [4] at lower NP density and attributed to the local recovery of AFM properties and interfacial coupling where two or more core-shell NPs are in contact. Such recovery can also be

effective for TriL 6.5, perhaps enhanced by the presence of a thick NiO film extending over the NPs (see Fig. 4). The consequent stronger coupling at the Ni/NiO interface (*i*) leads to increased magnetic anisotropy and T_B > RT and (*ii*) simplifies the energy landscape of the NP assembly by dwarfing the magnetostatic inter-NP interactions and thus preventing the formation of a spin-glass-like state, which only occurs when a multitude of energy minima is present.

The magnetization isotherms $M(H)$, measured at 5 K after field cooling (H_{cool} = +2 kOe), are shown in Fig. 9 and the corresponding magnetic parameters are collected in Table 2. All samples have an open $M(H)$ loop and are saturated before H reaches ±2 kOe, as expected for blocked NPs. The remanence/saturation M_{sr}/M_s ratio is close to the generally accepted value of 50% for blocked NPs, which are deemed to have uniaxial anisotropy due to surface effects irrespective of their crystal structure. The M_{sr}/M_s ratio confirms that the core-shell NPs are blocked at low temperature, in agreement with the shape of the magnetization isotherm. Before discussing coercivity H_c and EB field H_{bias}, it should be pointed out that these magnetic parameters must be obtained from major loops, where magnetic saturation is achieved at both loop extremes. Indeed, minor loops can be shifted in both horizontal (field) and vertical (magnetization) directions, thus preventing the meaningful derivation of coercivity and bias [37]. The loops shown in Figure 9 are major loops as they close before the min/max field (±2000 Oe) is reached and have no vertical shift. The only exception is the TriL 6.5 sample that has a hysteresis loop with a slight vertical shift. Therefore, its coercive and EB field values are slightly less accurate.

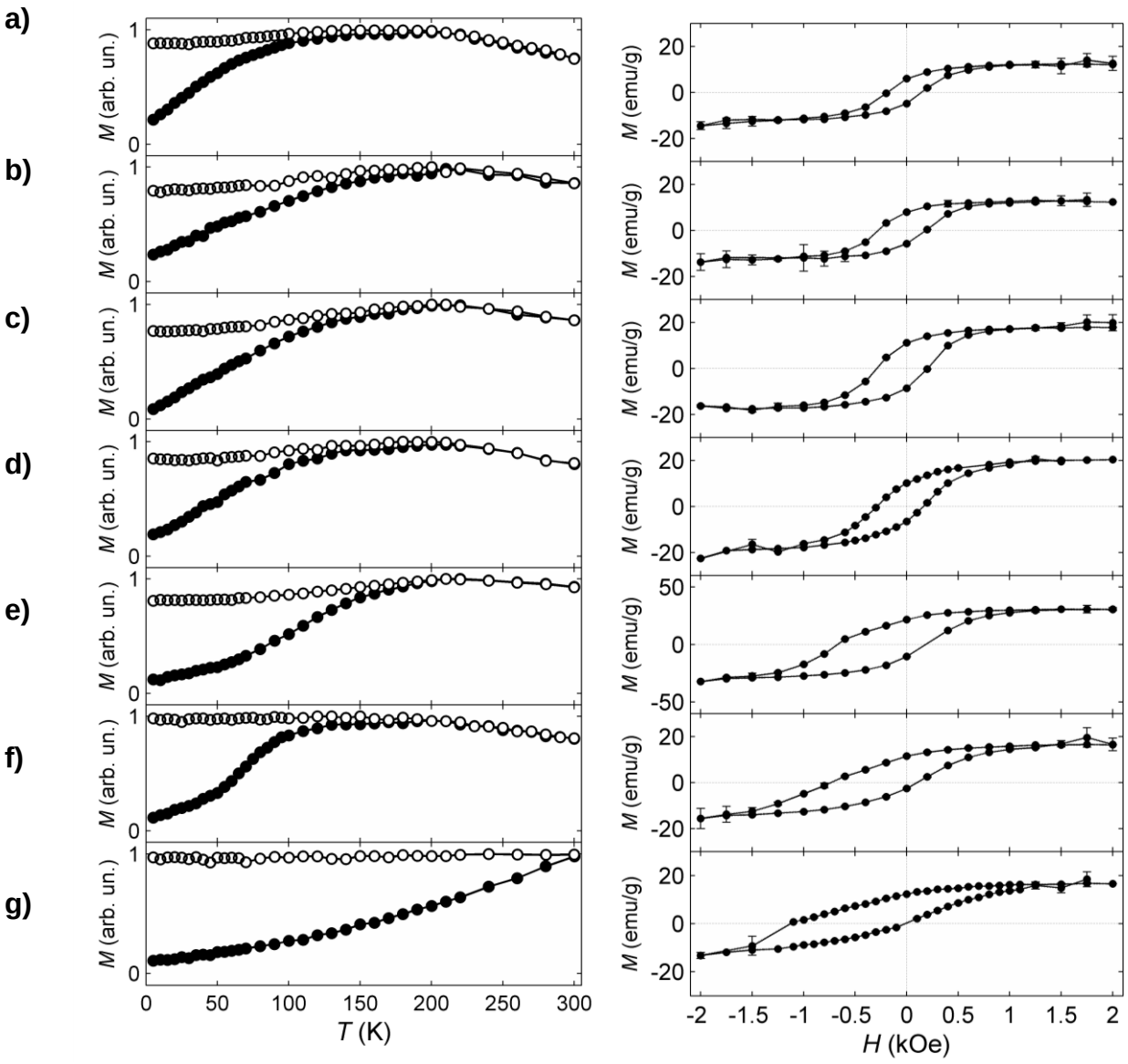

Figure 9. FC (hollow circles) and ZFC (solid circles) thermal magnetization curves (left) and FC magnetization isotherms (right, H_{cool} = +2000 Oe, T = 5 K) of Ni@NiO core-shell NPs. Magnetization M has been corrected for the support diamagnetic contribution and, in the case of magnetization isotherms, scaled to the nominal deposited nickel mass. a) TriL 0; b) TriL 0.3; c) TriL 0.67; d) TriL 1; e) TriL 2; f) TriL 3.5; g) TriL 6.5.

Table 2. Magnetic parameters of the Ni@NiO core-shell TriL NPs extracted from magnetization isotherms at $T = 5$ K.

Sample	TriL 0	TriL 0.33	TriL 0.67	TriL 1	TriL 2	TriL 3.5	Tril 6.5
M_s (emu/g) [a]	13.4	12.9	17.6	21.6	31.5	16.1	14.9
M_{sr} (emu/g) [a]	5.4	6.9	9.9	8.4	16.2	7.1	6.2
M_{sr} / M_s	0.40	0.56	0.56	0.39	0.51	0.44	0.42
H_{bias} (kOe)	0.022	0.045	0.043	0.062	0.25	0.31	0.57
H_{bias} / H_c	0.13	0.19	0.17	0.27	0.56	0.75	1.03
H_c (kOe)	0.17	0.23	0.25	0.23	0.44	0.42	0.55
H_{cr} (kOe)	0.27	0.32	0.32	0.37	0.58	0.70	0.89
H_{cr} / H_c	1.6	1.4	1.3	1.7	1.3	1.7	1.6
H_{cr}(+–) (kOe)	0.27	0.36	0.37	0.43	0.82	1.03	1.41
H_{cr}(–+) (kOe)	0.27	0.29	0.26	0.31	0.35	0.37	0.46

[a] Magnetization was scaled with respect to the nominal mass of deposited nickel.

The prominent shape change of the $M(H)$ isotherms with NiO shell thickness is reflected in the variation of H_c and H_{bias}, which are plotted *vs.* the corrected shell thickness t_s (cfr. Table 1) in Figure 10. The thickness of TriL 6.5 ($t_s \approx 5$ nm) has been linearly extrapolated using the thickness of samples TriL 1 to TriL 3.5. For comparison, the parameters of Ni@NiO NPs obtained by annealing [20] (Ann sample) are also plotted ($H_{bias} = 0.16$ kOe, $H_c = 0.31$ kOe, $H_{cr} = 0.81$ kOe); in this case the thickness of the NiO shell was estimated analyzing STEM images (cfr. Table 1). Coercivity H_c shows an increasing trend with t_s but its variation is irregular and hard to understand in detail. The EB field H_{bias} grows monotonically with increasing t_s. In detail, sample TriL 0 has a small but non vanishing H_{bias} because of the presence the underlying NiO first layer; a thin NiO layer, caused by oxidative processes that cannot be completely suppressed when the sample is exposed to air [18], can also be present. H_{bias} is slightly larger for TriL 0.33 and 0.67 where the NiO shell on the Ni NP is incomplete, as discussed in Subsection 3.3. From

TriL 1 on, H_{bias} increases with growing t_s without reaching a plateau. This steep increase is related to the growth of complete NiO shells around the Ni cores. The ratio H_{bias}/H_c is larger than 50% already for t_s = 2.3 nm and surpasses 100% for TriL 6.5, where NiO forms a discontinuous film embedding the Ni cores.

The EB effect in FM/AFM core-shell NPs depends on the thickness of the AFM layer because the anisotropy energy in the AFM layer $E_{an} = K\, t_s$ is proportional to the layer. In addition, a few magnetic parameters depend strongly on the AFM layer thickness [38], namely, the AFM anisotropy constant K itself (closely related to anisotropy field H_K), the Neél temperature T_N and the AFM blocking temperature $T_{B,AFM}$. Of course, the microscopic structure of the FM/AFM interface is of outstanding importance for the effectiveness of the EB effect but we assume that the highly-controlled synthetic method employed produced NPs with comparable interface structure. The importance of the interface quality for the exchange coupling can be appreciated by comparing the H_{bias} displayed by our TriL samples, for instance TriL 3.5 (H_{bias} = 0.31 kOe), with previous results on Ni@NiO NPs prepared by other methods involving the oxidation of preexisting metallic Ni NPs [20,21,39].

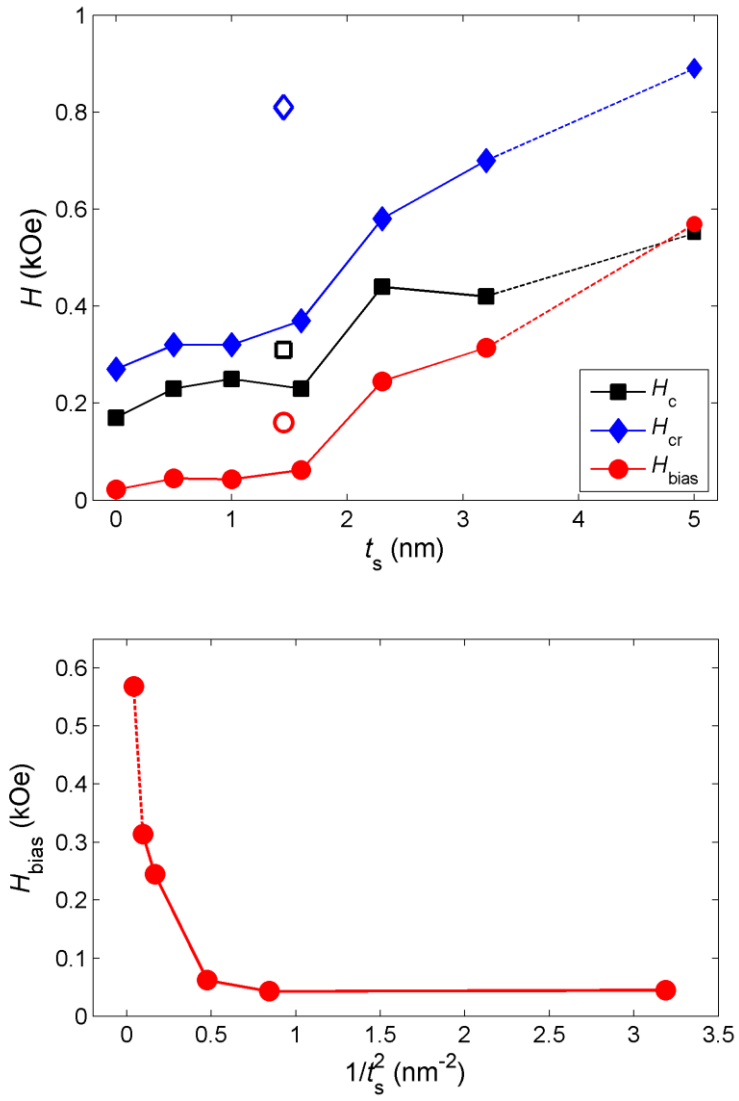

Figure 10. Dependence of the magnetic parameters of Ni@NiO core-shell NPs on the corrected NiO shell thickness t_s. The shell thickness of TriL 6.5 was extrapolated as denoted by the dashed lines. The shell thickness of the Ann sample was estimated from STEM images. (Top) Thickness dependence of coercivity H_c (black squares), remanence coercivity H_{cr} (blue diamonds), and bias field H_{bias} (red circles). TriL samples: solid markers; Ann sample: hollow markers. (Bottom) Dependence of H_{bias} of TriL samples on $1/t_s^2$.

It has been reported that T_N of NiO is close to RT already for $t_s \approx 1$ nm [40, 41] and that $T_{B,AFM}$ of NiO is often just a few tens of K below the T_N [42]. Thus, we focus our attention on the anisotropy energy E_{an} and the anisotropy constant K as parameters explaining how the shell thickness affects the EB. The linear dependence of E_{an} on t_s is the basis of the Meiklejohn-Bean approach [43], which neglects the thickness dependence of other magnetic parameters. Thus, it is useful to analyze the relationship between H_{bias} and t_s in the framework of the generalized Meiklejohn-Bean approach [44]. Within this model, H_{bias} is null when t_s is less than a critical value $t_{s,crit}$, then H_{bias} is proportional to t_s^{-2} for $t_s > t_{s,crit}$, with asymptotic value $H_{bias}(t_s \rightarrow \infty)$ for very large t_s. When the data of Table 2 are plotted as H_{bias} *vs*. t_s^{-2} (see Fig. 10b), one can see that the data are far from the simple linear dependence predicted by this model. Thus, in addition to E_{an}, the TriL samples differ in some magnetic parameter essential to the EB effect. A recent report [45] showed that the uniaxial anisotropy in a Fe/NiO bilayer grown on Au(001) is small for $t_s \leq 1.5$ nm, increases linearly from there to $t_s = 5.5$ nm up to $H_{Ku} = 150$ Oe, and is essentially constant afterwards. This behavior closely follows that displayed by H_{bias} of TriL samples and we therefore propose that the main contribution to the variation of H_{bias} in our TriL core-shell NPs can be ascribed to the increase of the NiO anisotropy constant as the shell thickness increases.

At equal shell thickness and Ni core size and density, the NPs obtained by annealing display larger H_c and H_{bias} than the TriL NPs (figure 10). For instance, the former reach $H_{bias}/H_c \approx 50\%$ for a thinner NiO shell ($t_s \cong 1.45$ nm), indicating that the Ni/NiO exchange coupling is more effective in these NPs. A few considerations focusing on the Ni/NiO interface can be made to explain this difference. In the annealed sample, the NiO shell grows along the [111] orientation.

The interface is thus uncompensated, comprising a layer of FM-coupled Ni^{2+}, and parallel to the spin alignment direction $[11\bar{2}]$ in bulk NiO (see figure S.2 in supplementary material). In the TriL samples, instead, it was observed that in some areas the NiO growth direction is [243], so the spins at the interface are compensated (figure S.4 in supplementary material) and only a small fraction of spins is expected to contribute to the interface exchange coupling [46]. It is however noteworthy that the [243] direction is perpendicular to the $[11\bar{2}]$ direction also in these samples. In addition to the interface type, one has also to consider the interface quality, which STEM and HR-TEM data showed to be much better in the annealed NPs due to the high-temperature treatment and to the lower NiO lattice expansion across the interface in the annealed (1%) than in TriL NPs (11%) (see supplementary material).

To gain more insight into the magnetic behaviour of TriL samples, we investigated the remanence coercivity H_{cr} (see Table 2) of the Ni@NiO NPs. H_{cr} is defined as the field corresponding to vanishing remanence and summarizes irreversible magnetization reversal better than H_c. H_{cr} was estimated by the ΔM method [47] as follows: First, the magnetization change due to irreversible processes was approximated as the difference $\Delta M = M_{desc} - M_{asc}$ between the two branches of the magnetization isotherm, then H_{cr} was estimated as the half width at half height (HWHH) of the peak-shaped ΔM curve (see Figure 11). In general, H_{cr} increases with increasing NiO shell thickness t_s in a way very similar to that of H_{bias} (see Fig. 10), similarly showing a slope change related to the formation of complete NiO shells on the Ni cores. This similarity supports the view that exchange coupling at the Ni/NiO interface is responsible for both the shift (H_{bias}) and the widening (H_c, H_{cr}) of the hysteresis loops. The remanence coercivity of ideal Ni NPs with effective uniaxial anisotropy can be estimated as $H_{cr} = 1.048\ |K_{Ni}|/M_s \cong 0.32$ kOe [47,48]. This value is in good agreement with the H_{cr} of samples TriL 0 to TriL 1, showing

that in these samples the NiO shell has little effect on the coercivity of the Ni core. The larger H_{cr} of TriL 2 to TriL 6.5 is evidence of the presence of higher barriers to magnetization reversal. The H_{cr} / H_c ratio ranges from 1.3 to 1.7 as predicted for single-domain NPs undergoing magnetization reversal by coherent rotation in the presence of a distribution of the coercivity of individual NPs [49].

The magnetic parameters H_{bias}, H_c, and H_{cr} are an attempt to summarize the magnetic behaviour of an assembly of NPs in a few numbers. A deeper insight may be achieved by investigating the micro-coercivity, *i. e.*, the barrier to magnetization reversal of individual NPs. The magnetization difference ΔM, which we used to estimate H_{cr}, is an approximation to the cumulative distribution of the micro-coercivity, also known as a cumulative remanence spectrum [50]. It can be found in Figure 11 along with the corresponding probability distribution, calculated as $|\mathrm{d}\Delta M/\mathrm{d}H|$. They are best discussed and understood by separately considering the left ($H \leq 0$) and right ($H \geq 0$) semi-plots. The left semi-plots picture the (cumulative) distribution of the micro-coercivity for the $+M$ to $-M$ reversal, *i. e.*, the reversal from the preferred alignment direction, set by interplay of the cooling field with the exchange interaction across the FM/AFM Ni/NiO interface, to the opposite direction. The right semi-plots represent the $-M$ to $+M$ reversal, where the Ni core magnetic moments regain the preferred orientation.

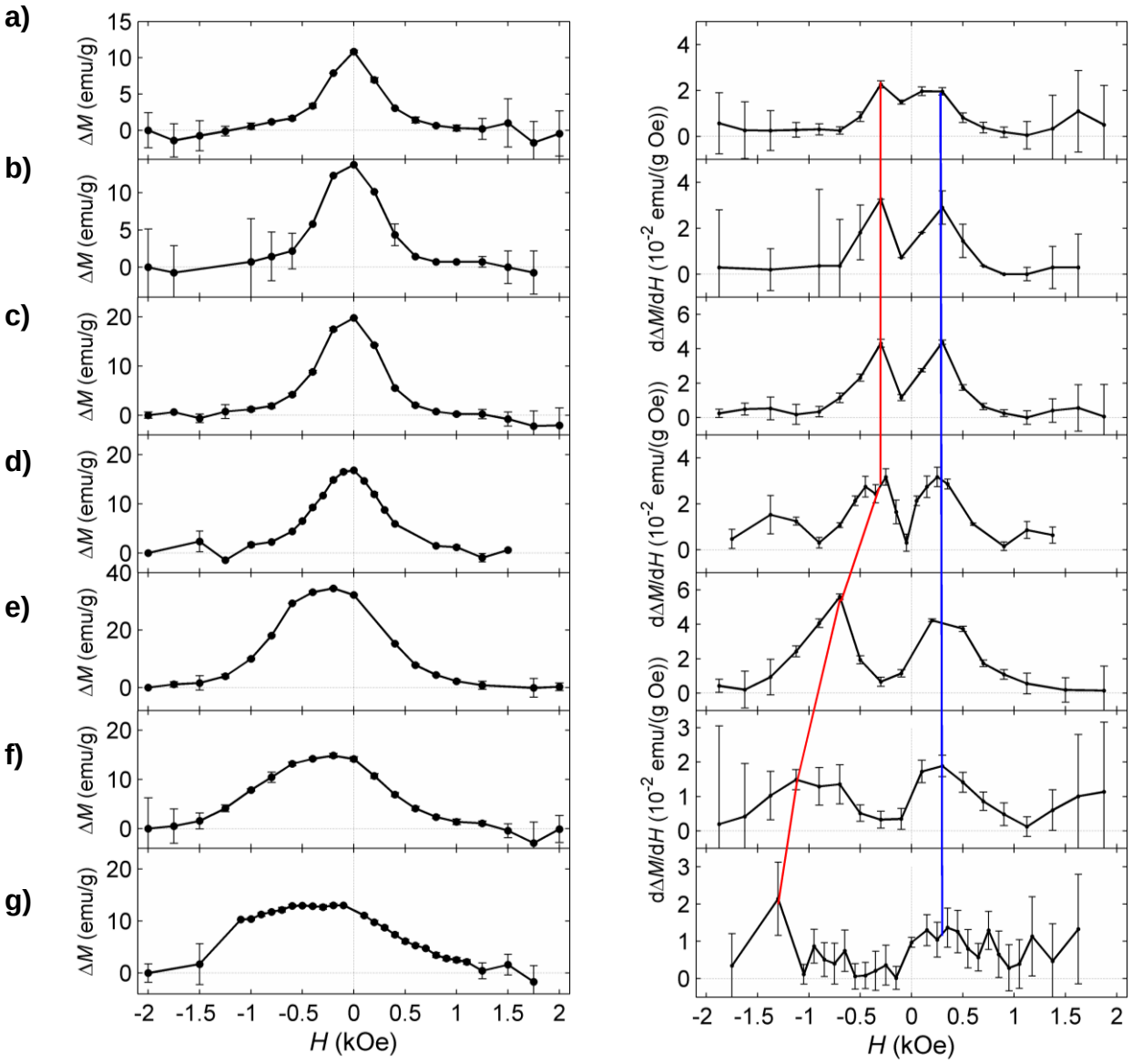

Figure 11. Remanence coercivity of the FC magnetization isotherms of Ni@NiO core-shell NPs calculated by the ΔM method. Left: cumulative remanence coercivity spectrum ΔM; right: remanence coercivity spectrum $|d\Delta M/dH|$. Both coercivity spectra have higher uncertainty than $M(H)$ isotherms in Fig. 9 due to error propagation in algebraic manipulation. The red line puts in evidence the shift of the maxima of $|d\Delta M/dH|$ for the ($+M$, $-M$) reversal; the blue line is for the

(–*M*, +*M*) reversal. a) TriL 0; b) TriL 0.3; c) TriL 0.67; d) TriL 1; e) TriL 2; f) TriL 3.5; g) TriL 6.5.

We first consider the +*M* to –*M* reversal ($H \leq 0$). The left Δ*M* semi-plot dramatically changes shape upon increasing NiO shell thickness: it substantially broadens, shifts toward more negative fields, and becomes flat in the (–1, 0) kOe range. The broadening can be quantified introducing the remanence coercivity for the –*M* to +*M* reversal H_{cr}(+–) as the HWHH of the left Δ*M* semi-spectrum (Table 2). The variation of H_{cr}(+–) as a function of t_s is similar to (but twice as steep as) that of H_{cr}. The most probable micro-coercivity corresponds to the maximum in the left |dΔ*M*/d*H*| semi-plot. The increase in NiO shell thickness is able to shift it by about 1 kOe from Tril 0 to Tril 6.5 (cfr. the red line in Fig. 10). In particular, it is almost constant at –0.4 kOe for the samples with small t_s (TriL 0 – TriL 1) and then progressively larger at –0.7 (TriL 2), –1.1 (TriL 3.5), and –1.3 kOe (TriL 6.5). Note also that for small t_s the coercivity distribution just shifts and broadens but when the NiO shell is thick (TriL 2 to Tril 6.5) there is a depletion of the probability of finding the individual NP coercivity in the range (–1, 0) kOe leading to a peaking of the coercivity distribution for the +*M* to –*M* reversal about –1.3 kOe. The coercivity distribution for the other reversal (–*M* to +*M*) is much less affected by the NiO shell thickness (right semi-plots in Fig. 11). The most remanence probable coercivity (+0.3 kOe) is unaffected by the NiO shell thickness (blue dashed line). An increase in H_{cr}(–+) from 0.26 to 0.46 kOe is observed in relation to a shape change of the right Δ*M* semi-plot featuring a larger probability for coercive fields in the (+0.5, +1) kOe.

4. Conclusions

The results of an investigation of morphology, chemical composition, structure and magnetism of core-shell Ni@NiO NPs have been presented. The NP assemblies were produced by sequential layer deposition using physical synthesis methods, in order to obtain ligand free nanosystems. The procedure consisted of the deposition of NiO layers on top of preformed 12 nm Ni NPs (obtained by making use of a magnetron and a gas aggregation chamber) sitting on a thin (1 nm) NiO layer by reactive evaporation of Ni from MBE cells in O_2 atmosphere. In this way, it was possible to investigate the evolution of morphology and magnetic properties of the NP assembly with different shell thickness and equal core size. These TriL samples comprise discrete Ni@NiO core-shell NPs, except for the sample with the thickest NiO top layer where an assembly of Ni NPs embedded in a discontinuous NiO matrix was obtained. TriL samples were compared to previously obtained core-shell Ni@NiO NPs prepared by annealing metallic Ni NPs in air. HR-TEM and STEM studies showed that the interface of TriL presents some regions where the interface is compensated with [243] orientation for the NiO growth (NiO lattice expansion 11%) whereas the annealed NPs have a sharper, uncompensated interface with [111] orientation for the NiO growth (NiO lattice expansion 1%).

The TriL samples displayed a small EB field H_{bias} up to t_s = 1.6 nm, but for thicker shells, H_{bias} is sizeable and steeply increasing without sign of saturation. At the thickest shell produced, H_{bias} = 0.57 kOe. This behavior can be related to the different morphology of the top NiO layer. At low deposited dose, NiO islands form and enlarge on the Ni cores, achieving a complete shell at t_s = 1.6 nm, and finally forming a discontinuous NiO matrix embedding the Ni cores. The thickness-dependence of H_{bias} cannot be explained by the generalized Meiklejohn-Bean model and the thickness dependence of the NiO anisotropy constant must be taken into account. The

importance of the interface type and quality for the effectiveness of the EB effect is put in evidence by comparison of the trilayer with the annealed core-shell NPs. The TriL samples have lower H_{bias} than the annealed sample of comparable NiO shell thickness due to the different arrangement and quality of the FM/AFM Ni/NiO interface. However, the trilayer samples bear a great advantage over the annealed NPs as the shell thickness can be varied at fixed core size. It is this last feature of the employed synthetic procedure that allowed us to separately investigate the thickness and interface contributions to the EB effect in Ni@NiO core-shell NPs. Furthermore, we demonstrated the viability of this method to obtain magnetic NPs with enhanced stability and showed that it is possible to tune the EB effect by the fine regulation of a "bulk" parameter, such as the AFM anisotropy. Our results are a first step in the direction of the rational design and synthesis of NPs with desired magnetic properties.

ACKNOWLEDGMENT

The authors gratefully acknowledge financial support by the Italian MIUR under grant FIRB RBAP115AYN (Oxides at the nanoscale: multifunctionality and applications). The Microscopy at ORNL was sponsored by the Office of Basic Energy Sciences, Division of Materials Sciences and Engineering, U.S. Department of Energy (MR), and by the European Research Council Starting Investigator Award (MR). SJP was supported by the Materials Science and Engineering Division of the US Department of Energy. G.C. Gazzadi is acknowledged for assistance in SEM experiments. Maria Varela is acknowledged for support.

REFERENCES

[1] Hao R, Xing R, Xu Z, Hou Y, Gao S and Sun S H 2010, *Adv. Mat.* **22** 2729

[2] Noguès J, Sort J, Langlais V, Skumryev V, Suriñaz S, Muñoz J S and Barò M D 2005 *Phys. Rep.* **422** 65

[3] Skumryev V, Stoyanov S, Zhang Y, Hadjipanayis G, Givord D and Nogués J 2003 *Nature* **423** 850

[4] Nogués J, Skumryiev V, Sort J, Stoyanov S and Givord D 2006 *Phys. Rev. Lett.*, **97** 157203

[5] Beans C P and Lingston J D 1959 *J. Appl. Phys.* **30** 1205

[6] Jiles D 1998 *Magnetism and Magnetic Materials* (London: Chapman and Hall)

[7] Sun S H, Murray C B, Weller D, Folks L and Moser A 2000 *Science* **287** 1989

[8] Martìn J I, Nogués J, Liu K, Vicent J L and Schuller I K 2003 *J. Magn. Magn. Mater.* **256** 449.

[9] D'Addato S, Gunnella R, Borgatti F, Felici R and Finetti P 2007 *Surf. Sci.* **601** 329

[10] Allia P, Coisson M, Spizzo F, Tiberti P and Vinai F 2006 *Phys. Rev. B* **73** 054409

[11] Meldrim J, Qiang Y, Liu Y, Haberland H and Sellmyer D J 2000 *J. Appl. Phys.* **87** 7013

[12] Binns C, Trohidou K N, Bansmann J, Baker S H, Blackman J A, Bucher J –P, Kechrakos D, Kleibert A, Louch S, Meiwes-Broer K -H, Pastor G M, Perez A and Xie Y 2005,*J. Phys. D: Appl. Phys*., **38** R357

[13] Kleibert A, Passig J, Meiwes-Broer K -H, Getzlaff M and Bansmann J 2007 *J. Appl. Phys.*, **101** 114318

[14] Binns C, Maher M J, Pankhurst Q A, Kechrakos D and Trohidou K N 2002 *Phys. Rev. B* **66** 184413

[15] D'Addato S, Grillo V, Altieri S, Frabboni S, Rossi F and Valeri S 2011 *J. Phys. Chem. C* **155** 14044

[16] Llamosa D, Ruano M, Martinez L, Mayoral A, Roman E, Garcia-Hernàndez M, Huttel Y 2014 *Nanoscale* **6** 13483

[17] D'Addato S, Gragnaniello L, Valeri S, Rota A, di Bona A, Spizzo F, Panozaqi T and Schifano S F 2010 *J. Appl. Phys.* **107** 104318

[18] D'Addato S, Grillo V, Altieri S, Tondi R, Valeri S and Frabboni S 2011 *J. Phys.: Condens. Matter* **23** 175003.

[19] D'Addato S, Grillo V, Altieri S, Frabboni S and Valeri S 2012 *Appl. Surf. Sci.* **260** 13.

[20] D'Addato S, Spadaro M C, Luches P, Grillo V, Frabboni S, Valeri S, Ferretti A M, Capetti E and Ponti A 2014 *Appl. Surf. Sci.* **306** 2.

[21] Johnston-Peck A C, Wang J and Tracy J B 2009 *ACS Nano* **3** 1077

[22] Ishizuka K 2013 *A Dedicated Site for Quantitative Electron Microscopy* http://www.hremresearch.com/

[23] Allen L J, McBride W, O'Leary N L and Oxley M P 2004 *Ultramicroscopy* **100** 91

[24] Grillo V and Rotunno E 2013 *Ultramicroscopy* **125** 97

[25] Schlager H G and von Löhneysen H 1997 *Europhys. Lett.* **40** 661

[26] Andres K**,** Bhatt R N, Goalwin P, Rice T M and Walstedt R E 1981 *Phys. Rev. B* **24** 244

[27] Giovanardi C, di Bona A and Valeri S 2004 *Phys. Rev. B* **69** 075418

[28] D'Addato S, Grillo V, di Bona A, Frabboni S, Valeri S, Lupo P, Casoli F and Albertini F 2013 *Nanotechnology* **24** 495703

[29] Mackay A L 1962 *Acta Cryst.* **15** 916

[30] Ino S 1969 *J. Phys. Soc. Jpn.* **27** 941

[31] Johnson C L, Snoeck E, Ezcurdia M, Rodrìguez-Gonzàlez B, Pastoriza-Santos J, Liz-Marzan R M and Hÿtch M J 2008 *Nature Mater.* **7** 120

[32] Gafner S L, Redel L V and Gafner Y Y 2007 *Phys. Met. Metallogr.* **104** 180

[33] Hÿtch M J, Snoeck E and Kilaas R 1998 *Ultramicroscopy* **74** 131

[34] Coey J M D 2010 *Magnetism and Magnetic Materials* (Cambridge: Cambridge University Press)

[35] Del Bianco L, Hernando A and Fiorani D 2005 *Surface Effects in Magnetic Nanoparticles* (New York: Springer) 217-238

[36] Bedanta S and Kleemann W J 2009 *J. Phys. D: Appl. Phys.* **42** 013001

[37] Geshev J 2008 *J. Magn. Magn. Mater.* **320** 600

[38] Lund M S, Macedo W A A, Liu K, Nogués J, Schuller I K and Leighton C 2002 *Phys. Rev. B* **66** 054422

[39] Zhou Y Z, Chen J S, Tay B K, Hu J F, Chow G M, Liu T and Yang P 2007 *Appl. Phys. Lett.*, **90** 043111

[40] Luches P, Benedetti S, di Bona A and Valeri S 2010 *Phys. Rev. B* **81** 054431

[41] Kim W, Jin E, Wu J, Park J, Arenholz E, Scholl A, Hwang C and Qiu Z Q 2010 *Phys. Rev. B* **81** 174416

[42] Nogués J and Schuller I K 1999 J. *Magn. Magn. Mater.* **192** 203

[43] Meiklejohn W H and Bean C P 1957 *Phys. Rev.* **105** 904

[44] Binek C, Hochstrat A and Kleemann W 2011 *J. Magn. Magn. Mater.* **234** 353

[45] Ma L Y, Chen G, Li J, Zhu J, Qiu Z Q and Wua Y Z 2012 *J. Magn. Magn. Mater*. **324** 528

[46] Takano K, Kodama R H, Berkowitz A E, Cao W and Thomas G 1997 *Phys. Rev. Lett.* **79** 1130

[47] Tauxe L, Mullender T A T and Pick T 1996 *J. Geophys. Res. Solid Earth* **101** 571

[48] Cullity B D and Graham C 2009 *Introduction to Magnetic Materials*, 2nd ed (USA: IEEE Press-Wiley)

[49] Dunlop D J and Özdemir Ö 1997 *Rock Magnetism* (Cambridge: Cambridge University Press)

[50] Jackson M, Worm H U and Banerjee S K 1990 *Phys. Earth Planet. Inter.* **65** 78